Heat and momentum transfer in microscale laminar fluid flow

Vânia Silvério[1], Viriato Semião[2] and António L. N. Moreira[3],

Universidade Técnica de Lisboa, Instituto Superior Técnico, Departamento de Engenharia Mecânica, Av. Rovisco Pais 1049-001 Lisboa, Portugal
[1,3]Centro Estudos em Inovação, Tecnologia e Políticas de Desenvolvimento, IN+
[2] Instituto de Engenharia Mecânica, IDMEC
email: vania.silverio@dem.ist.utl.pt http://in3.dem.ist.utl.pt/

Summary

The work reported here addresses an experimental study on the laminar transfer of heat and momentum in micro sizes tubes. The flow is set up by a syringe pump in borosilicate glass tubes heated by an electrical conductive transparent film of InO_x deposited in the channel outer wall, which allows establish a constant heat flux boundary layer at the same time that it provides optical access to the inner flow. The experiments encompass measurements of longitudinal distribution of temperature and pressure drop, complemented by velocity measurements of the inner flow with a MicroPIV system.

Keywords: *Microfluidics; Wettability; MicroPIV; Heat transfer*

1 Introduction

Systems miniaturization in diverse applications, either industrial or laboratorial, raises the need to better comprehend the scale effects induced on convective heat transfer inside micro tubes. Despite the extensive body of literature reported on these effects, experimental results are often influenced or even masked by several phenomenon, such as viscous dissipation [1], axial conduction along the walls [2], the validity of the slip-flow model [3] caused by molecular interactions at the surface-fluid interface [4] and/or by surface roughness effects [5, 6], or experimental uncertainties associated with channel dimensions [7], pumping power [8], pressure drop [9], entrance and exit effects [10], thermal boundary conditions [11], variation of fluid properties [12]). Moreover, studies of the flow inside micron-sized tubes mostly consider measurement of bulk flow parameters, such as pressure drop and spatial variations of mean temperature, which are often inconclusive about the existence of micro-scale effects. In this context, the micro Particle Imaging Velocimetry (μPIV) provides a valuable asset to assess the flow behavior, as it allows resolving the whole field [13] by scanning the measurement plane across the channel depth, [14].

The work addressed in the present paper combines pressure and temperature measurements with μPIV measurements, to evaluate the behavior to heat transfer of a microfluidic water flow in microchannels.

2 Experimental methodology

The experimental apparatus is schematically shown in Fig. 1. A constant mass flux of liquid (uncertainty, u = ±1%) is supplied at room temperature by a syringe pump NE-1000 from New Era Pump Systems, Inc®, with a Syringe B-D Perfusion 50/60mL (Inner Diameter, ID 27.12mm). Temperatures along the channel wall are measured with unsheated fine gage 25μm OD k-type thermocouples from Omega (u < ± 2%), attached along the channel outer wall with a non-conductive thermal glue (Cooler Master® PTK-002, thermal conductivity, k > 4.5W.m^{-1}.K^{-1}) to ensure a quick and reliable response and to minimize electrical conductance effects which would disturb the measurements. Thermocouples are also inserted at the inlet/outlet stagnation chambers. The ambient temperature is measured with a 1mm OD K-type thermocouple from Omega, placed near the channel inlet. Pressure losses are measured with two ECO1 pressure transducers from Wika (pressure, p = 0-4bar, u < ± 0.5%), located at the inlet and outlet stagnation chambers, respectively.

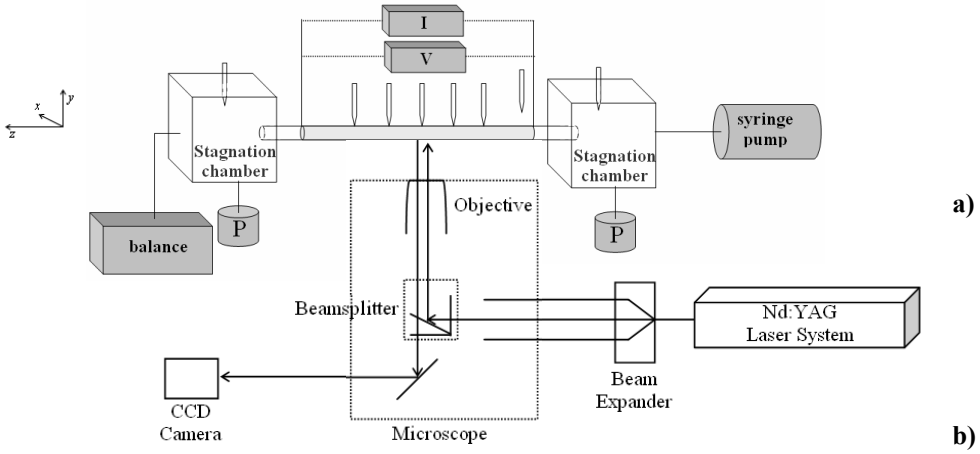

Fig. 1. Schematic of the **a)** flow delivery system; **b)** μPIV system

The microchannels are made of very smooth borosilicate glass from Vitrocom®, USA, with a rectangular cross section to minimize light refraction effects on μPIV measurements, as shown in the sample photo of Fig. 2 obtained with the Hitachi S_2400 scanning electronic microscope. Multi Image V2.1 software and Matlab® is used to assess the shape of the cross section and to accurately measure the inner and outer diameters of the channels (±4.4%).

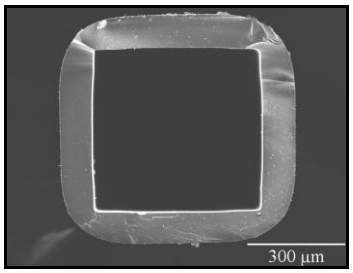

Fig. 2. SEM images of the S_500 cross section

The tubes are externally coated with a thin transparent film of Indium Oxide to provide heating by Joule effect at the same time it allows optical access to the inner flow. The process of deposition is described in [15]. Electrical contacts are achieved by means of electrically conductive silver containing acrylic paint, Elecolit® 340 (ρ < 0.001Ω.cm) and heating is provided by a direct current (GEN150-5, from TDK-Lambda, u < ±0.14%). Furthermore, temperature measurements made in the absence of inner flow, showed a constant value along the tube wall, which gives a clear indication that the thermal boundary condition approximates a constant heat flux condition (u < ±0.6%).

The experiments are conducted with distilled water, H_2O (IST Inorganic Chemistry Lab) and fluid properties are taken from the NIST Standard Reference Database 12 [16].

The μPIV system uses an inverted Leica DM ILM epi-fluorescent microscope and a Flowsense®_2M CCD (charge coupled device) camera from Dantec Dynamics to record 1μm average diameter nile red fluorescent tracing particles from Invitrogen® with an image field of 1600x1186 pixel^2 (pixel size 7.41μm) at a maximum rate of 15Hz and 8/10-bit intensity resolution. The particles are illuminated via a dual Nd:YAG laser New Wave_Solo II-15 emitting at λ=532nm with a repetition rate of 15Hz. The time delay between laser pulses is set between 100 and 500μs in which the particles have a maximum displacement of ¼ of the interrogation area length. An epi-fluorescent prism/filter cube is used to filter wavelengths lower than λ=575nm (particles wavelength emission) to prevent the influence of background noise. The field is magnified with an air-immersion N PLAN objective lens with magnification M=40 and numerical aperture NA=0.55.

FlowManager® V4.0 from Dantec Dynamics is used in acquisition, calculus and post processing of the data as well as in the correlation and validation algorithms. Synchronization is assured by National Instruments hardware.

Momentum and heat transfer data are obtained and processed as in [15]. The Poiseuille number, *f.Re*, for fully developed laminar flow of an incompressible fluid through a stationary smooth square cross sections is given by

$$f.Re = 56.92 \tag{1}$$

Where the Reynolds number $Re = \frac{\rho.u_m.D_h}{\mu}$ is defined with the hydraulic diameter $D_h=4A_{CS}/P$ and the bulk velocity $u_m = \dot{m}/\rho \cdot A_{CS}$ (μ is dynamic viscosity, ρ is the specific weight and $\dot{m}$ the mass flux. The Darcy friction factor *f* is then defined as

$$f = -\frac{dp}{dz}\frac{D_h}{\frac{1}{2}.\rho.u_m^2} \tag{2}$$

To obtain the pressure drop (*dp*) along the channel longitudinal distance *z*, pressure measurements are performed at the inlet and outlet plenums, as shown in Fig. 1a).

In data reduction, the flow is assumed laminar, incompressible, steady and fully developed (either hydrodynamically and/or thermally), gravity forces are ignored and the fluids are considered Newtonian. The 2D velocity distributions at any square cross section of inner dimension $\frac{1}{2}\Lambda_i$ and coordinate axes *(x,y)* with the origin at the center of the duct is given as [17].

$$u(x,y) = \frac{8\Lambda_i}{\mu\pi^3}\left(-\frac{dp}{dz}\right)\sum_{i=1,3,5,\ldots}^{\infty}(-1)^{\frac{i-1}{2}}\left[1-\frac{\cosh\left(\frac{i\pi y}{\Lambda_i}\right)}{\cosh\left(\frac{i\pi\frac{1}{2}\Lambda_i}{\Lambda_i}\right)}\right]\frac{\cos\left(\frac{i\pi x}{\Lambda_i}\right)}{i^3} \tag{2}$$

Velocity distributions are obtained by scanning the measurement plane across the depth of the tube and perpendicularly to the side wall by means of a stepper motor controlled by a real time RISC processor with reproducibility higher than 1μm and a total precision of ± 3μm,*e g.* Silva *et al.*, [18] – see Figure 1 -

The accuracy of the measurements is evaluated by comparing the volumetric flow rate yielded by the syringe pump with that obtained from the integration of the measured velocity distributions, as in [19].

Other potential sources of inaccuracy concern the suitability of the optical properties of the InOx deposit to obtain fluorescence measurements, as well of its chemical stability to provide accurate thermal boundary conditions. Most transparent conductors consist of metal oxides that possess both good electrical conductivity and transparency in the visible and near infrared (IR) regions of the electromagnetic spectrum. If transparent conductors/semiconductors thin films can be deposited at room temperature, transparent electronic devices can be laid upon any type of substrates, from glass to flexible polymers [20]. For heat transfer characterization, transparent un-doped conductor (electrical conductivity of about $1100\Omega^{-1}.cm^{-1}$) indium oxide film was deposited in the channel outer wall by radio frequency plasma enhanced reactive thermal evaporation (rf-PERTE) of indium at low substrate temperature (<100ºC). The film of InO_x is transparent (average visible transmittance of 81%) to allow optical access for laser based and visualization techniques. Details of the method and of the resulting relevant film chemical and physical properties are reported by Nunes de Carvalho *et al.* [21]. Only a summary is given here to contextualize the accuracy of the thermal boundary conditions. The source material (indium metal) is evaporated at steady state in the presence of oxygen inside a glass chamber at low temperature; the vapor is transported by thermal convection to the outer surface of the tube, which is placed horizontally 10cm apart. Rotation of the micro tube guarantees uniformity of the film thickness around the perimeter of the tubes and, therefore, of the electrical resistance. Even though, temperature measurements made by thermocouples randomly lined along the tube wall, revealed that any potential relation which would arise with the position of the tube in the stagnation chamber is statistically damped.

Moreover, the thin transparent film showed good chemical stability in the range of temperatures up to 70ºC, therefore indicating that the thermal boundary condition approximates a constant wall heat flux condition.

The heat flux transferred to the fluid, q''_s, is calculated from the Joule heating, q''_{eff}, taking into account the heat losses by convection, $q''_{loss}(z)$ and by radiation, q''_{rad} from the outer surface of the film to the environment as found in [15].

$$q''_s = q''_{eff} - q''_{loss} - q''_{rad} \tag{3}$$

The Nusselt number is then calculated from the heat transfer coefficient, h $\left(\equiv q_s^{"}/(T_i - T_m)\right)$ and the fluid thermal conductivity, k_{fl}

$$Nu = \frac{h D_h}{k_{fl}} \tag{4}$$

The pressure and temperature data are both acquired with a PCI-6024E/BNC-2120 data acquisition system from National Instruments and processed in MATLAB®.

3 Results and discussion

The application of analytical correlations usually well established for the friction factor and the Nusselt number at the "macroscale" (Fig. 3 and 4) show significant deviations to low Reynolds numbers in microscale flows.

Fig. 3 depicts the friction coefficient, *f*, for water as a function of the Reynolds number calculated with viscosity at room temperature for square cross section, for five different hydraulic diameters. The results show that scale effects are significant in smaller D_h channels, where friction in the water flows clearly deviates from the classical laminar theory for $Re < 100$.

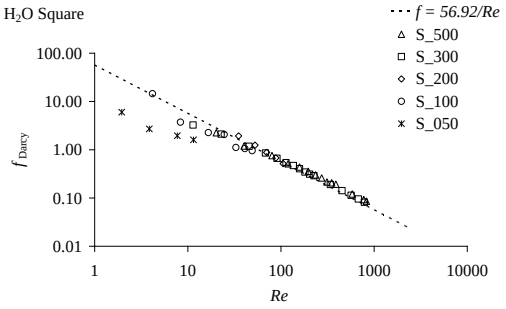

Fig. 3. Friction factor variation for distilled water in square cross section channels. ---- *f.Re*=constant

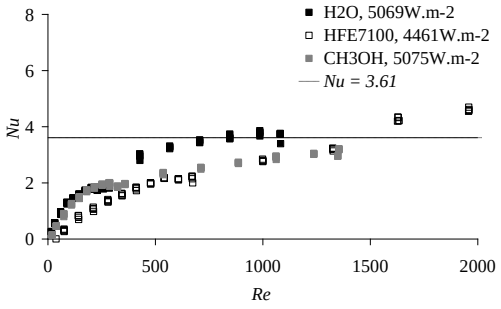

Fig. 4. Variation of the Nusselt number with the Reynolds number in fully developed flows.
Channel S_300; $q"_{eff} \approx 5000 Wm^{-2}$; ■ - water; □ - HFE7100; ■ - methanol

In Fig. 4, the average *Nu* is plotted against the Reynolds number for three fluids, water, methanol and HFE7100. The straight lines represent the *Nu* analytical value of 3.61 predicted by the laminar theory. The variations from "macroscale" are evident for all the fluids for lower Reynolds numbers.

These deviations are attributed to the lowering of the interfacial activity associated to the hydrophobic character of the channel internal wall induced by air pockets entrapped within the walls asperities [15], as observed by Moreira *et al.* [22] and by Bonaccurso *et al.* [23] in the flow of water in microtubes of glass.

Velocity measurements were performed at various heat fluxes (from about 3 to $20 kW.m^{-2}$) for the same inlet volumetric flow rate of $306 \mu L.s^{-1}$ and for the same heat flux of about $5900 W.m^{-2}$ at various inlet volumetric flow rates (31, 230 and $306 \mu L.s^{-1}$). Measurements are obtained far from the distance required for the flow to attain 99% of the fully developed centerline velocity, as given by $0.056 Re.D_h$, [24], such that the flow is surely fully developed. This is confirmed by comparing the mean velocity profiles taken at downstream locations. The flow is not expected to change in the streamwise direction across the length of the PIV image, unless there are spatial variations caused by surface roughness effects. The velocity fields were measured in several horizontal planes over the channel height (*y* direction).

The data plotted in Fig 5 and 6 is obtained with a time delay of 20μs between image pairs. Regarding the optimization of the signal-to-noise ratio, a time delay between laser pulses ranging from 100 to 300 μs and a repetition rate of 15 Hz are used to have a maximum particles displacement of approximately ¼ of the interrogation area extent. The PIV interrogation regions used here each contain an average of five particles ($8.28 \mu L$ particles to 1mL of deionized water corresponding to a concentration of $2.31 \times 10^8 particles.mL^{-1}$). This concentration of seed particles is small enough that any two-phase effects are considered negligible, and the working fluid can be considered a single-phase fluid. The time average correlation algorithm is applied over 100 correlation maps [25]. The lens used in the experiments has M=40 and NA= 0.55, which corresponds to a depth-

of-correlation value of 6.5μm [18]. In other words, particles up to ±3.25μm in front or behind the object plane may be enough in focus to be included in the measured velocity.

Fig. 5 shows the velocity vector field in the S_200 square cross-section borosilicate glass microchannel with an InO_x thin film deposited on the channel outer wall, acquired at ambient temperature. The mass flow inlet value was set to a value of $1.91x10^{-6}$ kg/s that corresponds to the volumetric flow rate of $115\mu L.min^{-1}$. The pressure at the inlet stagnation chamber to the microchannel system was set at 15.7KPa. The measurement volume is located 156μm from the bottom wall (40μm from the horizontal midplane). The Reynolds number of these flows based on hydraulic diameter and area-averaged velocity is 10.

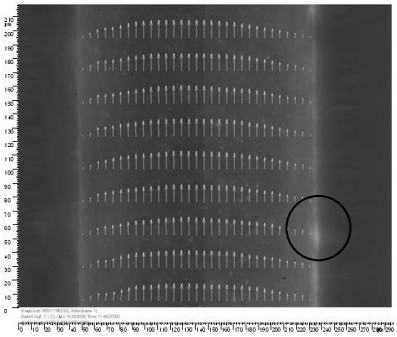

Fig. 5. Velocity vector field inside the S_200 microchannel for *Re* = 10 at the horizontal plane height *y*=40μm overlapping the microchannel image. Axial distance, z_0=28.21mm

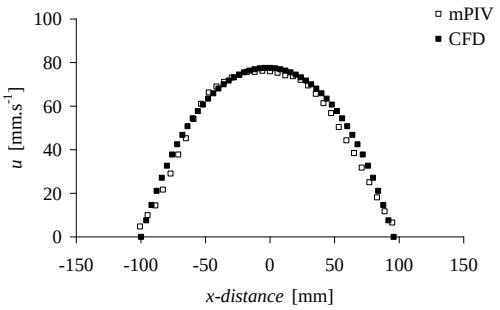

Fig. 6. Comparison between the measured velocity profile for S_200 microchannel for *Re*=10 at the horizontal plane height *y*=40μm (□), and the CFD analytical solution (■).

The interrogation regions for the measurements shown in Fig. 6 were 64 by 64 pixels with a 50% overlap in both the horizontal and vertical directions. Hence, a distance between individual vectors of 5.92 x 5.92 μm^2 was attained and measurements were found to be within 5.92μm of each wall.

The velocity measurements show the characteristic, approximately parabolic velocity field for fully developed pressure-driven liquid flow in a square microchannel. The consistency of vectors along the streamwise direction shows the fully developed flow. Measurements with μPIV are compared with CFD modeling results using Gambit® 2.2.30. A structured mesh with around $9x10^5$ hexahedron cells was used in the domain discretization, imposing control volumes sizes equal to those of the micro-PIV measurements. The numerical simulations (full squares) were performed with FLUENT® 6.2.16. The flow field was modeled as steady and laminar, and the inlet/outlet boundary conditions were set as mass flow inlet and outflow, respectively. The mass flow inlet value used was the experimental value of the volumetric flow rate provided by the syringe pump. Impermeable walls and the no-slip velocity condition at solid boundaries were applied to all the microchannel walls. Ambient temperature was considered.

The discrepancy between the PIV measurements and the predicted velocities is less than 1% near the center and increases to 12.6% for the measurements closest to the wall. The under-prediction of velocity for distances from ¼ of the channel to the wall is probably due to near-wall measurement effects. The hydrodynamic interactions between the particle and the wall and background reflections from the wall overshadow particle images. Although the InO_x thin film has an average visible transmittance of approximately 81%, it does not contribute in a significant manner to the overall error registered near the wall. The major contributors are the shape of the channel and particle agglomerates. The square channel has rounded exterior corners (Fig. 2) that can induce refraction near the walls [26] while particles agglomerates forming close to the walls, as can be seen inside the circle in Fig. 5, will contribute for the error in measurements due to their higher intensity emission. Techniques to improve PIV image interrogation near stationary interfaces are discussed by Theunissen *et al.* [27].

Fig. 7 shows the experimental flow velocity field acquired for the square channel with D_h of 522μm (S_500) at room temperature and the CFD result with Gambit®2.2.30 and numerical simulation with FLUENT®6.2.16. The results agree reasonably with the predicted velocity fields.

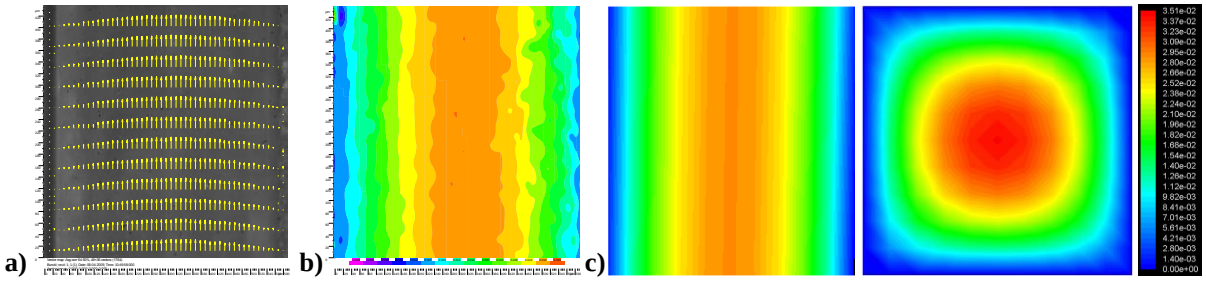

Fig. 7. Velocity fields for y=155µm obtained for S_500; q''_{eff} = 0 ; Q=306µL.min^{-1}
a) velocity mean vectors; **b)** isovelocity contours. **c)** Isovelocity contours obtained by CFD for the channel streamwise (y = 155µm) and transverse (z = 0.001m) planes.

Isovelocity maps acquired with FlowManager® V4.0 for experiments performed for constant heat fluxes of about 2600, 5900 and 8000W.m^{-2}, for the same mass flow inlet are to be seen in Fig. 8. In Fig. 9 the local velocity values in the streamwise direction are normalized by the average velocity value at the cross section under study, whereas the x-distance is normalized by the channel width, Λ_I. The plots in Fig. 9a) correspond to the experiments of Fig. 8 as for the results plotted in Fig. 9b) correspond to experiments in a different horizontal plane.

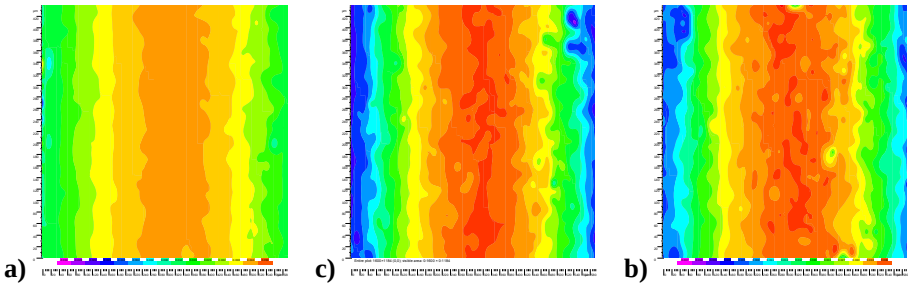

Fig. 8. Isovelocity maps for y=119µm obtained for S_500; Q=306µL.min^{-1}
a) $q''_{eff} \approx$ 2600Wm^{-2} **b)** $q''_{eff} \approx$ 5900Wm^{-2} e **c)** $q''_{eff} \approx$ 8000Wm^{-2}

Isovelocity contours and corresponding velocity profiles obtained for experiments present deviations when compared to those performed at room temperature. The increase of the velocity near the center region may be the result of the change in the wall characteristics and consequently the change in the fluid wall interaction. The adhesion forces, smaller at higher heat fluxes (due to the formation of nanobubbles adjacent to the channel wall [28]) induce the increase of velocity at the center of the channel.

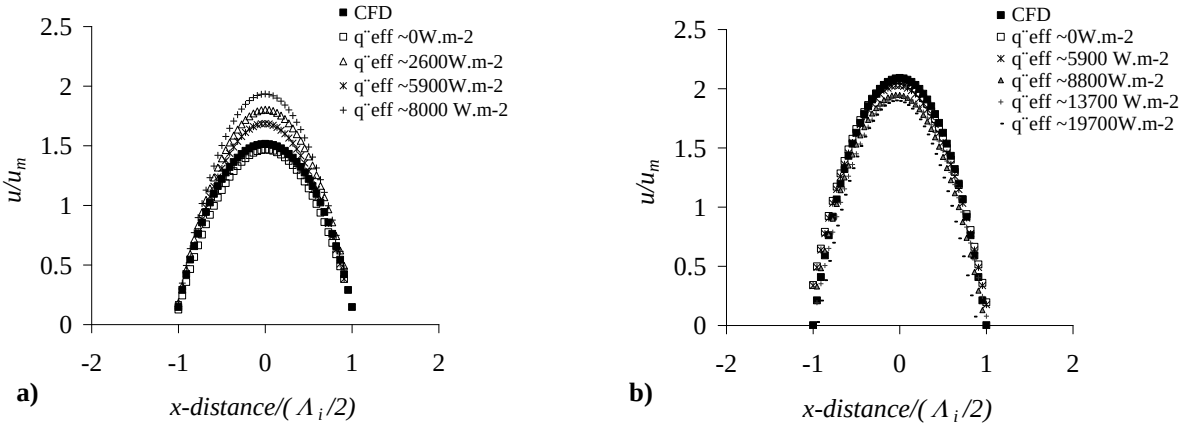

Fig. 9. Velocity profiles obtained for S_500 at different heat fluxes for **a)** y=119µm **b)** y=0µm; Q=306µL.min^{-1}

The results of tests carried out for a range of *Re* for the heat flux of approximately 5900W.s^{-2} are presented in Fig. 10. For each set of experiments, sufficient time was allowed to pass after starting the syringe pump to allow

the flow to reach steady-state. For smaller flow rates, it took a longer time to reach a steady-state compared to higher flow rates.

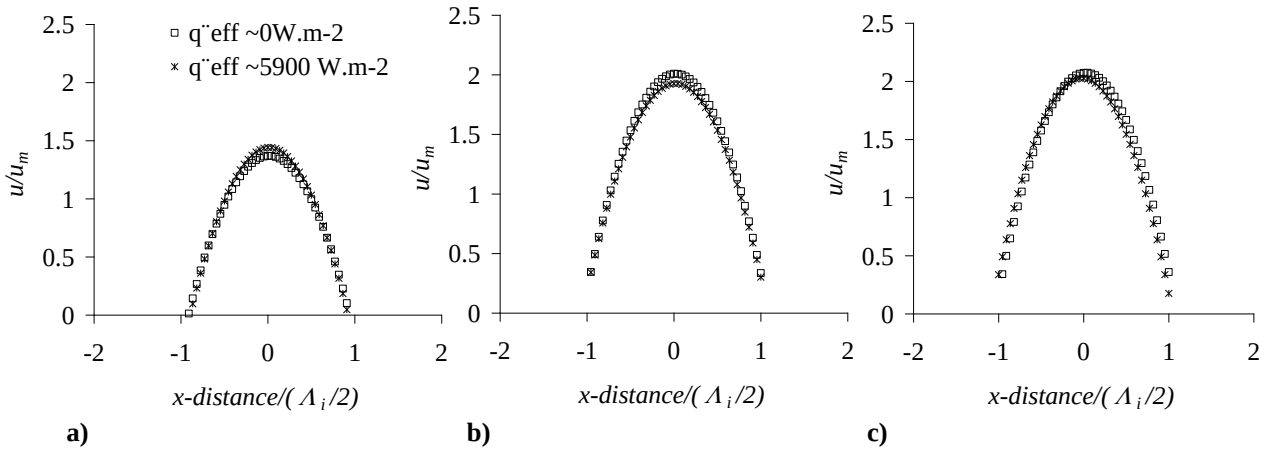

Fig. 10. Velocity fields of the channel obtained for S_500; $q''_{eff} \approx 0$ and 5900Wm^{-2}
a) y=165μm, Q=31μL.min^{-1} **b)** y=0μm, Q=230μL.min^{-11} **c)** y=0μm, Q=306.μL.min^{-1}

The numerical results fit well with the relation proposed by Martinelli and Viktorov in [30]. They state that for fully-laminar flow, the ratio between the maximum velocity at the midplane and the mean velocity (u_m) is 2.09.

4 Summary

The work reported in the present paper is part of a major experimental study concerned with the scale effects induced on the convection heat transfer inside micron sized tubes. The methodology combines previously reported temperature and pressure drop measurements with velocity distributions obtained with a Microscopic Particle Image Velocimeter (μPIV). The main goal of the analysis is to assess the suitability of the experimental methodology to identify and characterize the interfacial effects which have been suggested by the authors to inhibit heat and momentum transfer at reduced mass flow rates. The experiments consider the use of borosilicate microchannels of square cross section with hydraulic diameters of 195 and 522 mm, coated with a transparent metallic film to provide a constant wall heat flux at the same time it provides optical access for the use of visualization and laser diffraction techniques. Velocity measurements are reported for inlet volumetric flow rates of 31, 230 and 306μL.s^{-1} and heat fluxes from about 3 to 20kW.m^{-2}. Averaged velocity distributions and iso-velocity maps are calculated from the μPIV data.

The results evidence that the use of a InO_x thin film deposited on the channel outer wall is of major relevance for the application of the μPIV technique allowing to generate a constant heat wall heat flux with deviation smaller than 0,6% at the same time that it allows keeping high levels of transmittance (≈81%). Deviations of the velocity measurements are estimated to be smaller than 1% at the channel midplane, increasing to about 13% near the walls for S_200. Velocity distributions are further analyzed based on computational predictions performed with Fluent of the non-heated flow and the calculated values found to be in very good agreement with the experimental data for the channel midplane, though deviations increase at planes in the vicinity of the channel walls.

The results clearly show an increase of the mean velocity gradient at the tube wall with the heat flux, in detriment of a decrease at the middle plane. Though not clear, the experimental evidence is in accordance with previous findings that the flow approaches a non-slip condition for which heat and momentum transfer is inhibited due to the formation of a layer of nanobubbles between the wall and fluid. Thus, care must be taken in the usage of non degassed fluids for the air entrapped may significantly change the wettability and hence the heat transfer in microchannels.

5 Acknowledgments

The authors gratefully acknowledge the financial support of the Portuguese Science and Technology Foundation. They thank to Professor Nunes de Carvalho and his team for the enlightenment on InO_x thin film deposition. They also wish to thank Gonçalo Silva and João Costa for all the help with the CFD computations.

6 References

[1] G.L. Morini and M. Spiga, The role of the viscous dissipation in heated microchannels, Transactions of the ASME 129 (2007) 308-318.

[2] D. Lelea, The conjugate heat transfer of the partially heated microchannels, Heat and Mass Transfer 44 (2007) 33–41.

[3] L. Kuddusi and E. Çetegen, Prediction of temperature distribution and Nusselt number in rectangular microchannels at wall slip condition for all versions of constant heat flux, International Journal of Heat and Fluid Flow 28 (2007) 777-786.

[4] C.D. Meinhart, Surface/fluid interactions in micro & nano-channels, (2007), AFSOR FA9950-04-0106.

[5] P. Hrnjak and X. Tu, Single phase pressure drop in microchannels, International Journal of Heat and Fluid Flow 28 (2007) 2-14.

[6] G. Croce, P. D'Agaro and C. Nonino, Three-dimensional roughness effect on microchannel heat transfer and pressure drop, International Journal of Heat and Mass Transfer 50 (2007) 5249–5259.

[7] M.E. Steinke and S.G. Kandlikar, Single-phase liquid friction factors in microchannels, International Journal of Thermal Sciences, 45 (2006) 1073-1083.

[8] A. Husain and K.-Y. Kim, Optimization of a microchannel heat sink with temperature dependent fluid properties, Applied Thermal Engineering 28 (2008) 1101–1107.

[9] G. D. Ngoma and F. Erchiqui, Heat flux and slip effects on liquid flow in a microchannel, International Journal of Thermal Sciences 46 (2007) 1076–1083.

[10] G. Gamrat, M. Favre-Marinet and D. Asendrych, Conduction and entrance effects on laminar liquid flow and heat transfer in rectangular microchannels, International Journal of Heat and Mass Transfer 48 (2005) 2943–2954.

[11] K. Horiuchi and P. Dutta, Joule heating effects in electroosmotically driven microchannel flows, International Journal of Heat and Mass Transfer, 47(14-16) (2004) 3085-3095.

[12] J.-T. Liu, X.-F. Peng and W.-M. Yan, Numerical study of fluid flow and heat transfer in microchannel cooling passages, International Journal of Heat and Mass Transfer 50 (2007) 1855–1864.

[13] S.T. Wereley and C.D. Meinhart, Micro- and nano-scale diagnostic techniques. K. Breuer (Ed.), Springer Verlag, 2005, NY

[14] J.G. Santiago, S.T. Wereley, C.D. Meinhart, D.J. Beebe and R.J. Adrian, A particle image velocimetry system for microfluidics, Experiments in Fluids 25 (1998) 316-319.

[15] V. Silvério and A.L.N. Moreira, Friction losses and heat transfer in laminar microchannel single-phase liquid flow, 6th Int. Conference in Nanochannels, Minichannels and Microchannels, ASME, Darmstadt, 2008.

[16] E.W. Lemmon, M.O. McLinden and M.L. Huber, NIST standard reference database 12, V5.2, US Secretary of Commerce, USA, 2005.

[17] F.M. White, Viscous fluid flow, McGraw-Hill, 1974, 119-125

[18] G. Silva, N. Leal and V. Semião, Micro-PIV and CFD characterization of flows in a microchannel: velocity profiles, surface roughness and Poiseuille numbers, International Journal of Heat and Fluid Flow, 29 (2008) 1211–1220.

[19] G. Silva, N. Leal and V. Semião, Determination of microchannels geometric parameters using micro-PIV, Chemical Engineering Research and Design, *in press*.

[20] C. Liu, T. Matsutani, N. Yamamoto and M. Kiuchi, High-quality indium tin oxide films prepared at room temperature by oxygen ion beam assisted deposition, Europhys. Lett. 59 (4) (2002) 606.

[21] C. Nunes de Carvalho, G. Lavareda, P. Parreira, J. Valente, A. Amaral and A.M. Botelho do Rego, Influence of oxygen partial pressure on the properties of undoped InO_x films deposited at room temperature by rf-PERTE, Journal of Non-Crystalline Solids, 354 (2008) 1643–1647.

[22] A.L.N. Moreira, A.S. Moita, E. Cossali, M. Marengo and M. Santini, Secondary atomization of water and isooctane drops impinging on tilted heated surfaces, Experiments in Fluids 43(2-3) (2007) 297-313.

[23] E. Bonaccurso, M. Kappl and H.-J. Butt, Hydrodynamic force measurements: boundary slip of water on hydrophilic surfaces and electrokinetic effects, Physical Review Letters 88(7) (2002) 076103.

[24] J.H. Spurk and N. Aksel, Fluid mechanics, 2nd Ed., Springer-Verlag, Germany, 2008, pp.268

[25] C.D. Meinhart, S. Wereley and J.G. Santiago, A PIV algorithm for estimating time-averaged velocity fields, Journal of Fluids Engineering, 122 (2000) 285-289.

[26] F.A. Jenkins and H.W. White, Fundamentals of optics, International Student Edition, 4th ed., McGraw-Hill, 1981, 44-59.

[27] R. Theunissen, F. Scarano and M.L. Riethmuller, On improvement of PIV image interrogation near stationary interfaces, Experiments in Fluids 45 (2008) 557–572.

[28] M. Martinelli and V Viktorov, Modelling of laminar flow in the inlet section of rectangular microchannels, Journal of Micromechanics and Microengineering 19 (2009) 025013